Heterogeneous Slowdown of Dynamics in the Condensate of an Intrinsically Disordered Protein

Saumyak Mukherjee and Lars V. Schäfer*

Center for Theoretical Chemistry, Ruhr University Bochum, 44780 Bochum, Germany

E-mail: lars.schaefer@ruhr-uni-bochum.de

Abstract

The high concentration of proteins and other biological macromolecules inside biomolecular condensates leads to dense and confined environments, which can affect the dynamic ensembles and the time scales of the conformational transitions of the biomolecules. Here we use atomistic molecular dynamics (MD) simulations on the intrinsically disordered low complexity domain (LCD) of the human fused in sarcoma (FUS) RNA-binding protein as a model system to study how self-crowding inside a condensate affects the dynamic motions of the protein. We found a heterogeneous retardation of the protein dynamics, with large-amplitude motions being strongly slowed by up to two orders of magnitude, whereas small-scale motions, such as local backbone fluctuations and side-chain rotations, are less affected. The results support the notion of a liquid-like character of the condensates and show that different protein dynamic modes exhibit differential sensitivity to the crowded environment.

The discovery of membraneless organelles (MLOs) has changed cellular biophysics,[1] challenging the traditional view that cellular compartmentalization is exclusively mediated by lipid-bound organelles and vesicles. MLOs are high-density liquid droplets formed through the process of liquid-liquid phase separation (LLPS)[2–6] of proteins, particularly intrinsically disordered proteins (IDPs),[7,8] and RNA.[9] They play critical roles in orchestrating various cellular processes.[3,10–13] For example, the biochemical reactions occurring in MLO compartments are crucial for transcription, stress response, synaptic activity, RNA splicing, receptor-mediated signalling, and mitosis.[14–22]

Due to their ability to concentrate biological molecules, MLOs are described as biomolecular condensates or biocondensates.[23] The concentrations of proteins and/or nucleic acids inside the condensates are typically higher than 100 mg mL^{-1}.[24–27] This leads to increased viscosity inside the droplets, which can be 3 to 6 orders of magnitude larger than dilute solutions.[28] Consequently, the diffusion of biomolecules in condensates is strongly retarded.[24,25,29–33] For example, a 500-fold decrease of translational diffusion in the condensates was reported for the intrinsically disordered low-complexity domain (LCD) of the human fused in sarcoma (FUS) RNA-binding protein.[25]

The dynamic and broad conformational ensembles of IDPs, as dictated by their amino acid sequences, lead to dynamic multivalent interactions that play a key role in driving LLPS and stabilizing biocondensates.[5,34] In general, the flat free-energy landscapes of IDPs imply lack of a stable persistent conformation, but a highly dynamic conformational ensemble that is characterized by rapid transitions between a multitude of metastable minima.[35,36] This plasticity of IDPs[37] fosters dynamic interactions in the condensates, which includes mechanisms such as folding-upon-binding, formation of highly dynamic biomolecular complexes, conformational selection, and fly casting.[38–41] Some of these mechanisms involve the transient formation of (local) structure, via the restriction of certain dynamic conformational modes.[28] The increased viscosity in condensates is expected to further restrict the conformational dynamics of the proteins, although they can still be highly dynamic.[42,43]

To fulfil their biological functions, biocondensates need to ensure a high local concentration certain biomolecules. At the same time, these biomolecules need to retain their dynamic nature as much as possible, and such liquid-like character is also crucial for the dynamic exchange of molecules between condensates and their surrounding. The dynamic nature of condensates partly originates from the high degree of conformational flexibility of the constituent IDPs, fostered also by the relatively high water content of the droplets.[25,44,45] Driven by this plasticity and the lack of membranes the condensates can rapidly form, reshape and adapt their properties, and hence efficiently interact and exchange molecules with their surroundings.[46] The precise link between the dynamical nature of condensates and their biological functions can be challenging to establish, and may strongly depend on the particular system under investigation.[13,47] For example, Fischer et al. recently showed that transcription factor condensates with more liquid-like character lead to higher gene expression levels than stiffer condensates.[48] Taken together, it is important to characterize and understand the dynamical behavior of biomolecules in condensates at various time- and length scales.

Here we focus on the effect of crowding on the protein dynamics in condensates formed by the intrinsically disordered low complexity domain (LCD) of the human fused in sarcoma (FUS) RNA-binding protein.[24,27,49] FUS is physiologically important for RNA shearing and transport, DNA repair, micro-RNA processing, gene transcription, and regulation.[50–52] The LCD region is primarily responsible for driving LLPS.[24,25,27,53,54] It encompasses the N-terminal 163 residues of the 526 residues long protein. It is rich in polar glutamine and serine residues, tyrosines, and also glycines, which are known to be important for condensate formation via LLPS.[55]

In this work, we use all-atom MD simulations to study the dynamics of the protein backbone and side-chains of FUS-LCD condensates and compare them to dilute conditions (snapshots of the systems are shown in Figure S1). We observed a correlation between the length- and time scales associated with the dynamical slowdown in the crowded environment

of the condensates. The results portray a heterogeneous dynamical retardation of the protein motions at different length scales. Furthermore, the effect of self-crowding on the dynamics of water molecules in the protein hydration layer was studied.

To understand the effects of crowding in the condensates on the dynamics of the protein chains, the backbone and side-chain motions were investigated separately. First, the overall translational dynamics of the FUS-LCD chains were characterized by calculating the mean square displacements (MSD) of the C_α atoms in the protein backbone. Figure 1A shows the MSD averaged over all the C_α atoms present in the dilute (red) and the condensate (blue) systems plotted as a function of the lag time.

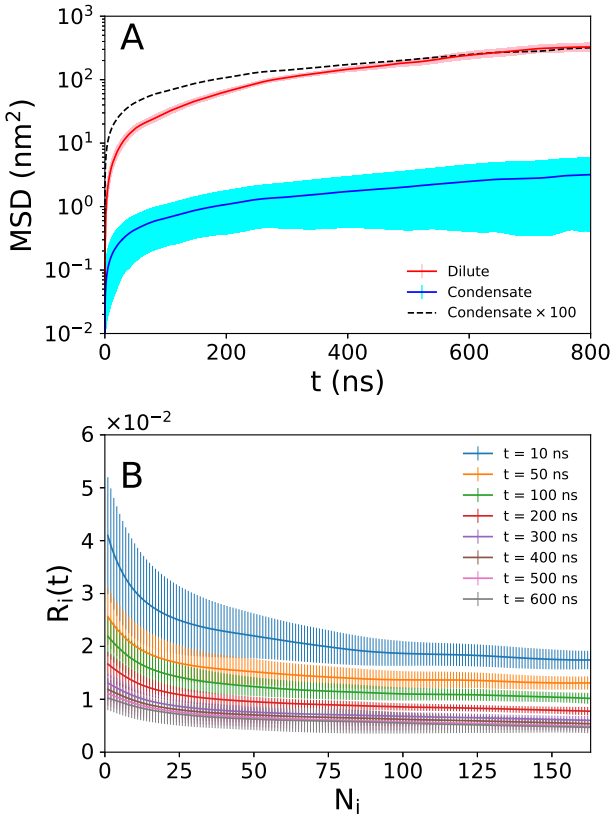

Figure 1: A) Mean square displacements of C_α atoms in the protein backbones in the dilute (red) and condensate (blue) systems plotted as a function of the lag time t. The semi-log plot enables a clearer comparison between the slower and faster dynamics in the condensate and the dilute systems. The solid lines represent the mean MSD and the error bars denote the standard deviations over all the C_α atoms considered. The black dashed line represents the condensate MSD multiplied by 100. B) Ratio of the mean MSDs of C_α atoms in the condensate and the dilute systems at selected lag times (10, 50, 100, 200, 300, 400, 500, 600 ns) plotted against the number of C_α atoms in a group. The error bars denote the standard deviations over the 8 protein chains present in the simulation system.

From Figure 1A an average translational slowdown of two orders of magnitude can be observed from the dilute to the condensate phase (the black dashed line represents the mean MSD of the C_α atoms in the condensate multiplied by 100). To analyze this slowdown in further detail, MSDs of groups of increasing numbers of consecutive C_α atoms in the FUS-LCD chain were calculated, with group sizes ranging from a single C_α atom to the whole chain (163 C_α atoms)

$$MSD_i(t) = \frac{1}{N_i} \sum_{j=1}^{N_i} (\vec{x}_j(t) - \vec{x}_j(0))^2 \tag{1}$$

In equation 1, $\vec{x}_j(0)$ and $\vec{x}_j(t)$ denote the position vectors of the jth C_α atom at a time origin and at a lag time t later, respectively. Each group of size N_i (the number of C_α atoms in the ith group) has $163 - N_i + 1$ instances or subgroups, and the MSD was calculated by averaging over all these subgroups.

Figure 1B shows the ratio

$$R_i(t) = \frac{MSD_{i,cond}(t)}{MSD_{i,dil}(t)} \tag{2}$$

of MSD_i in the condensate and the dilute system as a function of N_i at selected lag times. A lower value of $R_i(t)$ indicates a stronger slowdown of dynamics in the condensate phase. As shown in Figure 1B, at larger lag times, the dynamical retardation is more pronounced compared to smaller lag times. Additionally, larger groups of atoms experience a greater slowdown. Consequently, the MSD of smaller groups of atoms at shorter lag times exhibits the least dynamical retardation. The differences in $R_i(t)$ diminish as one progresses to larger lag times, indicating that the retardation as a function of lag time is nonlinear and that beyond a certain point, the dynamics are similarly slowed down.

This analysis demonstrates that the motions of larger masses on longer length scales (as expected at longer lag times) through the crowded condensate environment are subject to stronger dynamic retardation.

The above analysis provides a measure of the retardation of the translational motions of the protein backbone in the condensate. To more closely understand this dynamic slowdown, the reorientation motions of the protein backbone were analyzed, separately from the side-chains. This was achieved by studying the reorientation of the vectors between two C_α atoms at varying sequence separations.

First, the orientational autocorrelation functions (ACFs)

$$C_{or}(t) = \frac{\langle \vec{\mu}(0) \cdot \vec{\mu}(t) \rangle}{\langle \vec{\mu}(0) \cdot \vec{\mu}(0) \rangle} \tag{3}$$

were calculated for the $C_\alpha - C_\alpha$ vectors $\vec{\mu}(t)$ at different separations ($N_{C_\alpha - C_\alpha} = 1$ to 162), averaged over all possible instances of $N_{C_\alpha - C_\alpha}$. The brackets $\langle \ldots \rangle$ indicate the average over all time step differences t. The ACF in Eq. 3 describes the reorientation motion of the $C_\alpha - C_\alpha$ vectors via the angle θ_t formed by a vector during the time interval t. The mean ACFs were fitted to biexponential functions (Eq. 4) and the mean orientational time scales (Eq. 5) were obtained by integration

$$C_{or}(t) = \sum_{i=1}^{2} a_i \exp\left(-\frac{t}{\tau_i}\right) + \left(1 - \sum_{i=1}^{2} a_i\right) \tag{4}$$

$$\tau_{or} = \sum_{i=1}^{2} a_i \tau_i \tag{5}$$

The amplitudes a_i were normalized to obtain relaxations between 1 and 0. ACFs for selected $C_\alpha - C_\alpha$ separations are shown in Figure S2. The applicability of the biexponential fit was decided by calculating the R^2 (coefficient of determination) values at each separation and comparing mono-, bi-, and triexponential fits (Figure S3). The triexponential fits were not superior to the biexponential ones, so we select the biexponentials.

The same approach was taken to quantify the magnitude or distance fluctuations of the $C_\alpha - C_\alpha$ vectors

$$C_{mag}(t) = \frac{\langle |\vec{\mu}(0)| \cdot |\vec{\mu}(t)| \rangle}{\langle |\vec{\mu}(0)| \cdot |\vec{\mu}(0)| \rangle} \tag{6}$$

where $|\vec{\mu}(0)|$ and $|\vec{\mu}(t)|$ are the magnitude of the vector at time origin and at a lag time t later, respectively. Also in this case, biexponential functions accurately described the relaxations (Figures S4 and S5).

Figures 2A and 2B show the orientational time scales for the dilute (τ_{dil}^{or}) and the conden-

sate (τ^{or}_{cond}) systems, respectively. The ratio of the two time constants is shown in Figure 2C. Figures 2D, 2E, and 2F show the analogous graphs for the $C_\alpha - C_\alpha$ distance fluctuations. The relaxation time scales in this case are denoted by τ^{mag}_{dil} and τ^{mag}_{cond} for the dilute and the condensate phase, respectively.

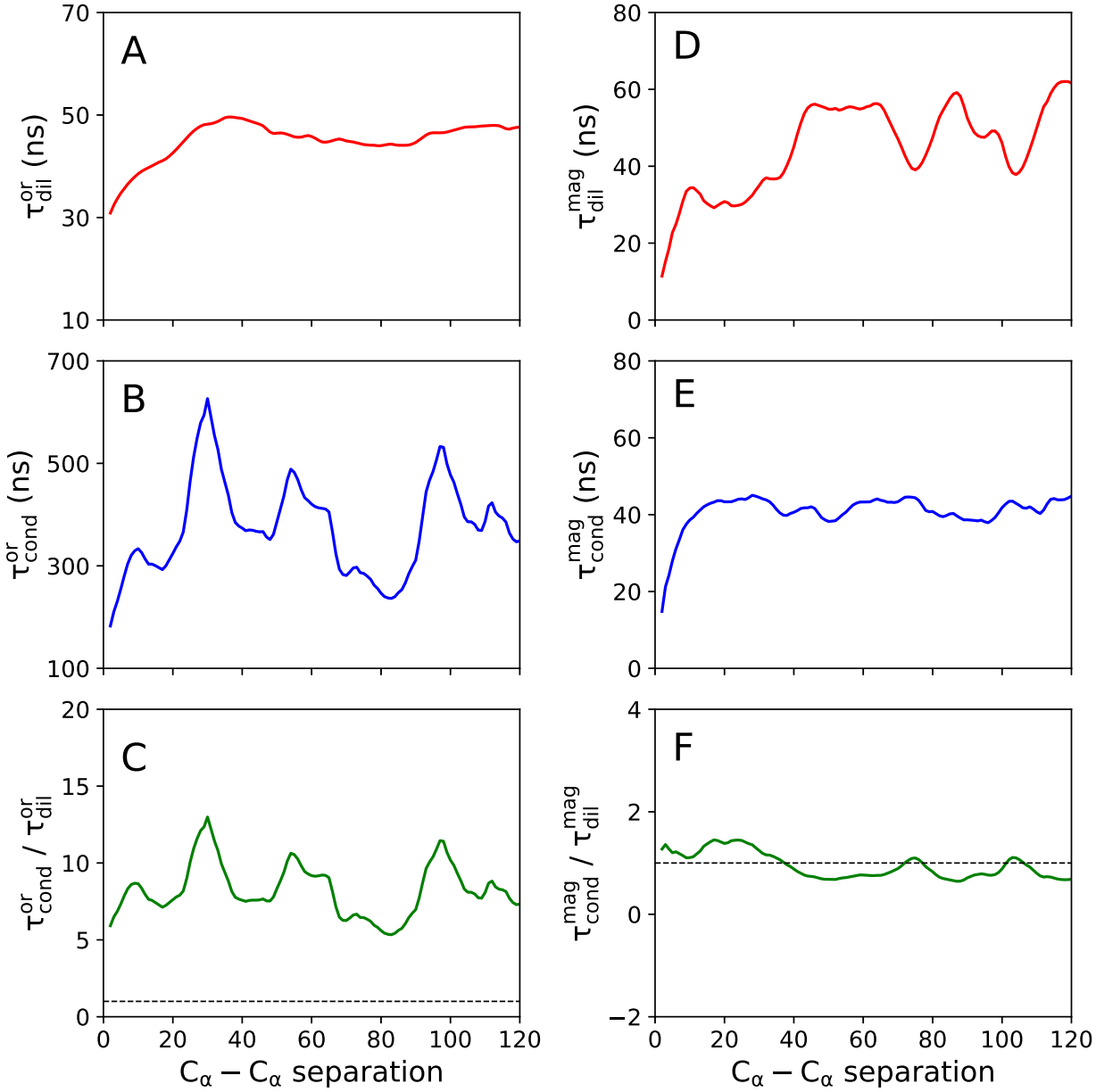

Figure 2: Protein backbone dynamics for FUS-LCD chains. A) and B) represent the time scales of orientational dynamics as a function of $C_\alpha - C_\alpha$ separation for the dilute and the condensate systems respectively. C) represents the ratio of these two time scales. D), E), and F) show the analogous properties for the $C_\alpha - C_\alpha$ distance fluctuations.

Figure 2A shows that retardation of orientational backbone dynamics is observed with an increase in $N_{C_\alpha - C_\alpha}$. At longer length scales (sequence separation $N_{C_\alpha - C_\alpha} > 40$), the value of τ_{dil}^{or} plateaus. A qualitatively similar behavior is also observed for τ_{dil}^{mag} (Figure 2D). A smooth $N_{C_\alpha - C_\alpha}$ dependence is found for τ_{cond}^{mag} (Figure 2E), while τ_{cond}^{or} (Figure 2B) shows larger variations.

The time scale ratio depicted in Figure 2C illustrates that the orientational dynamics of the backbone are slowed down by factors of approximately 5-15 (about one order of magnitude) in the condensate compared to the dilute system. In contrast, the $C_\alpha - C_\alpha$ distance dynamics exhibit no noticeable slowdown in the condensate system (Figure 2F). This apparent contradiction can be resolved by considering the nature of dynamical variables analyzed. While the reorientation dynamics of the protein backbone involves motions of backbone atoms through a dense and viscous environment, the distance magnitude fluctuations pertain to the local motions of the C_α atoms around their average positions. Thus, in the context of the above results on the retardation of global protein translational dynamics (see previous section), we conclude that protein dynamics involving large-scale motions are more strongly affected by the crowded environment provided by the condensate phase.

Next, we investigate the motions of the amino acid side-chains in terms of rotamer jumps. The dynamics of the side-chains were analyzed by computing the normalized time ACFs $C_\chi(t)$ of the dihedral angles χ_i ($i = 1, 2, 3$, depending on the length of the side-chain)

$$C_{\chi_i}(t) = \frac{\langle \cos \chi_i(0) \cdot \cos \chi_i(t) \rangle}{\langle \cos \chi_i(0) \cdot \cos \chi_i(0) \rangle} \tag{7}$$

For each amino acid occurring in the FUS-LCD sequence that at least has the χ_1 dihedral (ASN, ASP, GLN, SER, THR, and TYR), for each χ_i, the ACFs (Eq. 7 were averaged over all the side-chains present in the system. These mean ACFs were fitted by biexponential functions (Eq. 4) and integrated (Eq. 5) to obtain the relaxation times, which are plotted in Figure 3. The individual ACFs are shown in Figures S6 and S7. Biexponential functions accurately describe the ACFs (Figure S8).

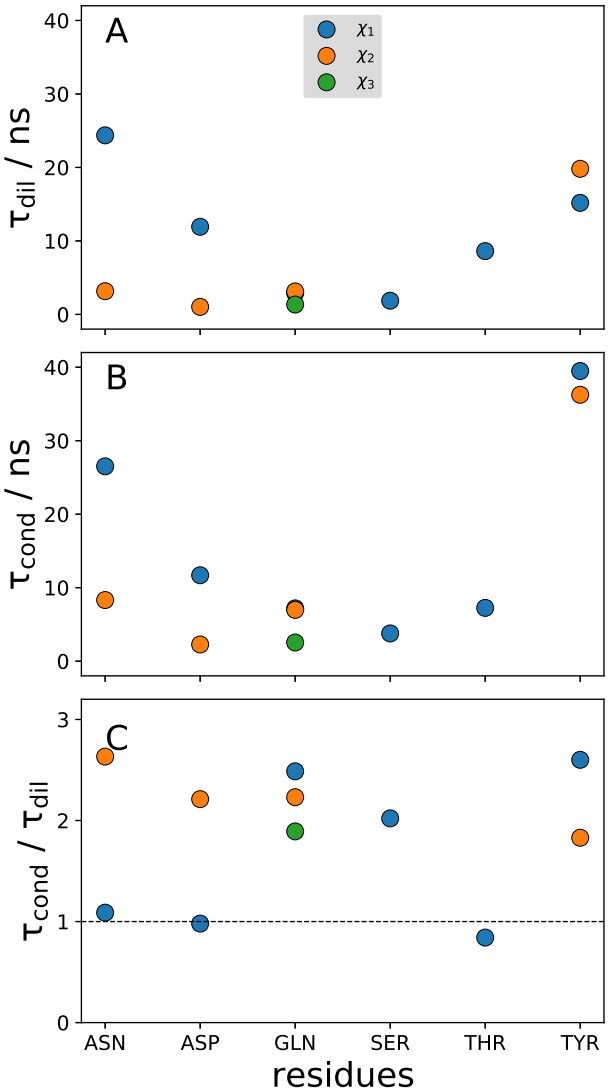

Figure 3: Time scales of side-chain dihedral angle rotations in the dilute (A) and the condensate (B) systems. C) shows the ratio of the time constants in the two systems. The χ_1, χ_2, and χ_3 dihedral angles of the respective residues are plotted in blue, orange, and green, respectively.

Figures 3A and 3B present the time scales in the dilute (τ_{dil}) and the condensate (τ_{cond}) systems, respectively. The ratio of τ_{cond} and τ_{dil} is shown in Figure 3C. The side-chain dynamics are not significantly slowed in the condensate. Averaged over all side-chains and dihedral angles (χ_1, χ_2, χ_3), the retardation is about twofold. This small change is similar to the backbone $C_\alpha - C_\alpha$ magnitude fluctuations reported above, supporting the notion that local fluctuations do not experience a pronounced slowdown in the condensate. The time

scales of the small-amplitude protein motions are thus largely unaffected in the condensate.

Finally, we analyzed the dynamics of water molecules in the protein hydration layer (PHL), as they are coupled to protein dynamics.[56–63] To investigate the effect of the altered protein dynamics in the crowded environment of the condensate on the hydration water dynamics, the reorientation motions (rotations) of the water molecules in the PHL were probed, which was defined as the region within 0.5 nm of the protein surface. To quantify the water reorientation motions in the PHL, we computed the time ACFs of the dipole moment vector of each water molecule (Eq. 3). In this case, $\vec{\mu}(t)$ denotes the normalized dipole moment vector of a single water molecule (for a rigid water model, as used in this work, an O-H bond vector (and not the dipole moment) can be used for the analysis). As described above, the ACFs were fitted to biexponential functions and integrated to obtain the rotational relaxation times. The distributions of the time scales obtained for the dilute and condensate phases are plotted in Figure 4A.

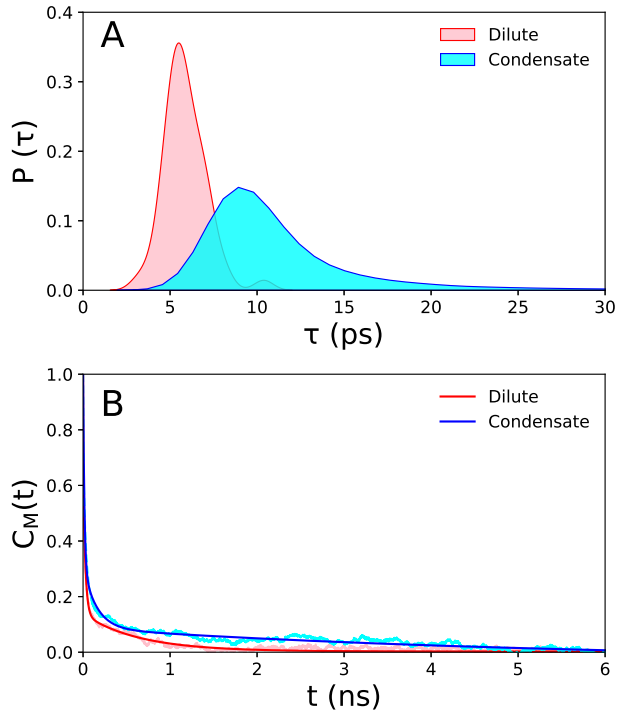

Figure 4: Dynamics of protein hydration layer (PHL) in the dilute (red) and condensate (blue) phases. The PHL is defined by a cut-off distance of 0.5 nm from the protein. A) Distributions of 1st-order rotational ACF relaxation times. B) ACFs of total dipole moment of PHL in the dilute and condensate phases.

Figure 4A shows that the time scale distribution for the condensate system is broader compared to the dilute phase. This indicates a partial slowdown in the rotational dynamics of water in the PHL within the condensate. The mean relaxation times for the dilute and the condensate systems are 6 ps and 12 ps, respectively. Hence, the water dynamics in the condensates is slowed down by a factor of two.

While the above analysis provides a measure of the dynamical slowdown at the level of single water molecules, a more global picture can be drawn by comparing the collective relaxation of the entire protein hydration layer, as described by the ACF of the total dipole moment $C_M(t)$ (Eq. 8).

$$C_M(t) = \frac{\left\langle \delta\vec{M}(0) \cdot \delta\vec{M}(t) \right\rangle}{\left\langle \delta\vec{M}(0) \cdot \delta\vec{M}(0) \right\rangle} \tag{8}$$

In equation 8, the total dipole moment fluctuation is denoted by $\delta\vec{M}(t) = \vec{M}(t) - \left\langle \vec{M} \right\rangle$, where $\vec{M}(t) = \sum_{i=1}^{N} \vec{\mu}_i(t)$ is the total dipole moment vector of the PHL, $\left\langle \vec{M} \right\rangle$ denotes the time-averaged dipole moment, and $\vec{\mu}_i(t)$ is the dipole moment of the ith water molecule in the PHL. The $C_M(t)$ of the dilute (red) and the condensate (blue) phases are plotted in Figure 4B. The dashed lines represent the raw ACFs, whereas the solid lines denote their fits. In this case, a triexponential function provided better fits ($R^2_{dil} = 0.93$ and $R^2_{cond} = 0.96$) than a biexponential function ($R^2_{dil} = 0.91$ and $R^2_{cond} = 0.92$).

The average relaxation times thus obtained are 101 ps and 670 ps for the dilute and the condensate systems, respectively. Hence the collective water relaxation is slowed by a factor of 6.7. The hydration water analysis thus shows that single-molecule rotational water motions are slowed down twofold, while overall collective dynamics of the ensemble of hydration water molecules is affected to a greater extent. These findings support the results of Reid et al. that the relaxation of the PHL of IDPs is slow and more heterogeneous.[64]

In general, slowed water dynamics and a concomitant stiffening of the water H-bond network are linked to reduced water entropy.[65–69] The associated changes of solvation thermodynamics can be sizeable in magnitude, especially when the water molecules are constrained by the strongly confined environment in the dense biocondensate[70,71] Vibrational spectroscopy studies have shown that the slowed water is associated with the retardation of dynamic modes of the biomolecules, which couple to the PHL.[72,73] However, even at condensate concentrations as high as 300 mg/ml and beyond, the water volume fraction is still relatively large, ensuring that the condensates retain a liquid-like character that maintains a high degree of biomolecular dynamics.

In conclusion, in this work we probed the dynamic slowdown of an intrinsically disordered protein and the water in its hydration layer in condensates using atomistic MD simulations. The crowded milieu in the dense condensate phase slows down both protein and water dynamics, but to markedly different extents depending on the length scale of the motions involved. The retardation of dynamics is non-universal and heterogeneous, with dynamic

modes that involve mass transfer over long length scales or large-amplitude motions being affected more strongly than small-scale local fluctuations.

The most significant dynamical retardation of almost two orders of magnitude is found for the translational motions of the backbone (measured by the MSDs of the C_α-atoms). The slowdown increases with increasing number of atoms in the translating group. For small-amplitude motions such as fluctuations of distances between pairs of C_α atoms in the IDP backbone and side-chain dihedral rotations, the dynamical slowdown by the condensate is not significant. However, the orientational dynamics of $C_\alpha - C_\alpha$ vectors, which require movement of the atoms through the crowded condensate interior, are found to be slowed down by almost one order of magnitude.

The hydration layer water dynamics, probed by single molecule rotational ACF, does not show any substantial slowdown in the condensate. However, a much stronger effect is seen in the collective dynamics of hydration water in terms of total dipole moment ACF.

Taken together, this work enhances our atomic-level understanding of the structural dynamics and their modulation in IDP condensates, as investigated here for FUS-LCD as a case example. The correlation found between the dynamic slowdown and the associated length scales might be transferable to other biocondensates, and hence have more general implications beyond the specific IDP studied in this work.

Acknowledgements

This project received funding from the European Union's Horizon 2020 research and innovation programme under the Marie Skłodowska-Curie grant agreement No 801459 - FP-RESOMUS and from the Deutsche Forschungsgemeinschaft (DFG) under Germany's Excellence Strategy - EXC 2033 - 390677874 - RESOLV.

Supporting Information Available

Methods (system set-up and simulation details); Selected ACFs for $C_\alpha - C_\alpha$ reorientation dynamics for selected separations in the condensate system; R^2 values plotted against $C_\alpha - C_\alpha$ separations for reorientation dynamics in dilute and condensate systems for different fitting functions; Selected ACFs for $C_\alpha - C_\alpha$ distance fluctuations for selected separations in condensate system; R^2 values plotted against $C_\alpha - C_\alpha$ separations for distance fluctuations in dilute and condensate systems for different fitting functions; ACFs of side-chain rotamer dynamics in dilute and condensate systems; R^2 values for different fitting functions in the side-chains dynamics ACFs.

References

(1) Brangwynne, C. P.; Eckmann, C. R.; Courson, D. S.; Rybarska, A.; Hoege, C.; Gharakhani, J.; Jülicher, F.; Hyman, A. A. Germline P granules are liquid droplets that localize by controlled dissolution/condensation. *Science* **2009**, *324*, 1729–1732.

(2) Shin, Y.; Brangwynne, C. P. Liquid phase condensation in cell physiology and disease. *Science* **2017**, *357*, eaaf4382.

(3) Alberti, S.; Gladfelter, A.; Mittag, T. Considerations and challenges in studying liquid-liquid phase separation and biomolecular condensates. *Cell* **2019**, *176*, 419–434.

(4) Dignon, G. L.; Best, R. B.; Mittal, J. Biomolecular phase separation: From molecular driving forces to macroscopic properties. *Annu. Rev. Phys. Chem.* **2020**, *71*, 53–75.

(5) Pappu, R. V.; Cohen, S. R.; Dar, F.; Farag, M.; Kar, M. Phase Transitions of Associative Biomacromolecules. *Chem. Rev.* **2023**, *123*, 8945–8987.

(6) Mittag, T.; Pappu, R. V. A conceptual framework for understanding phase separation and addressing open questions and challenges. *Mol. Cell* **2022**, *82*, 2201–2214.

(7) Li, Q.; Peng, X.; Li, Y.; Tang, W.; Zhu, J.; Huang, J.; Qi, Y.; Zhang, Z. LLPSDB: a database of proteins undergoing liquid–liquid phase separation in vitro. *Nucleic Acids Res.* **2020**, *48*, D320–D327.

(8) Wang, X.; Zhou, X.; Yan, Q.; Liao, S.; Tang, W.; Xu, P.; Gao, Y.; Li, Q.; Dou, Z.; Yang, W.; others LLPSDB v2.0: an updated database of proteins undergoing liquid–liquid phase separation in vitro. *Bioinformatics* **2022**, *38*, 2010–2014.

(9) Liu, M.; Li, H.; Luo, X.; Cai, J.; Chen, T.; Xie, Y.; Ren, J.; Zuo, Z. RPS: a comprehensive database of RNAs involved in liquid–liquid phase separation. *Nucleic Acids Res.* **2022**, *50*, D347–D355.

(10) Song, D.; Jo, Y.; Choi, J.-M.; Jung, Y. Client proximity enhancement inside cellular membrane-less compartments governed by client-compartment interactions. *Nat. Commun.* **2020**, *11*, 5642.

(11) Poudyal, R. R.; Guth-Metzler, R. M.; Veenis, A. J.; Frankel, E. A.; Keating, C. D.; Bevilacqua, P. C. Template-directed RNA polymerization and enhanced ribozyme catalysis inside membraneless compartments formed by coacervates. *Nat. Commun.* **2019**, *10*, 490.

(12) Klein, I. A.; Boija, A.; Afeyan, L. K.; Hawken, S. W.; Fan, M.; Dall'Agnese, A.; Oksuz, O.; Henninger, J. E.; Shrinivas, K.; Sabari, B. R.; others Partitioning of cancer therapeutics in nuclear condensates. *Science* **2020**, *368*, 1386–1392.

(13) Lyon, A. S.; Peeples, W. B.; Rosen, M. K. A framework for understanding the functions of biomolecular condensates across scales. *Nat. Rev. Mol. Cell Biol.* **2021**, *22*, 215–235.

(14) Banjade, S.; Rosen, M. K. Phase transitions of multivalent proteins can promote clustering of membrane receptors. *eLife* **2014**, *3*, e04123.

(15) Strom, A. R.; Emelyanov, A. V.; Mir, M.; Fyodorov, D. V.; Darzacq, X.; Karpen, G. H. Phase separation drives heterochromatin domain formation. *Nature* **2017**, *547*, 241–245.

(16) Wang, A.; Conicella, A. E.; Schmidt, H. B.; Martin, E. W.; Rhoads, S. N.; Reeb, A. N.; Nourse, A.; Ramirez Montero, D.; Ryan, V. H.; Rohatgi, R.; others A single N-terminal phosphomimic disrupts TDP-43 polymerization, phase separation, and RNA splicing. *EMBO J.* **2018**, *37*, e97452.

(17) Woodruff, J. B. Assembly of mitotic structures through phase separation. *J. Mol. Biol.* **2018**, *430*, 4762–4772.

(18) von Appen, A.; LaJoie, D.; Johnson, I. E.; Trnka, M. J.; Pick, S. M.; Burlingame, A. L.; Ullman, K. S.; Frost, A. LEM2 phase separation promotes ESCRT-mediated nuclear envelope reformation. *Nature* **2020**, *582*, 115–118.

(19) Chen, X.; Wu, X.; Wu, H.; Zhang, M. Phase separation at the synapse. *Nat. Neurosci.* **2020**, *23*, 301–310.

(20) Protter, D. S.; Parker, R. Principles and properties of stress granules. *Trends Cell Biol.* **2016**, *26*, 668–679.

(21) Boehning, M.; Dugast-Darzacq, C.; Rankovic, M.; Hansen, A. S.; Yu, T.; Marie-Nelly, H.; McSwiggen, D. T.; Kokic, G.; Dailey, G. M.; Cramer, P.; others RNA polymerase II clustering through carboxy-terminal domain phase separation. *Nat. Struct. Mol. Biol.* **2018**, *25*, 833–840.

(22) Hnisz, D.; Shrinivas, K.; Young, R. A.; Chakraborty, A. K.; Sharp, P. A. A phase separation model for transcriptional control. *Cell* **2017**, *169*, 13–23.

(23) Banani, S. F.; Lee, H. O.; Hyman, A. A.; Rosen, M. K. Biomolecular condensates: organizers of cellular biochemistry. *Nat. Rev. Mol. Cell Biol.* **2017**, *18*, 285–298.

(24) Burke, K. A.; Janke, A. M.; Rhine, C. L.; Fawzi, N. L. Residue-by-residue view of in vitro FUS granules that bind the C-terminal domain of RNA polymerase II. *Mol. Cell* **2015**, *60*, 231–241.

(25) Murthy, A. C.; Dignon, G. L.; Kan, Y.; Zerze, G. H.; Parekh, S. H.; Mittal, J.; Fawzi, N. L. Molecular interactions underlying liquid- liquid phase separation of the FUS low-complexity domain. *Nat. Struct. Mol. Biol.* **2019**, *26*, 637–648.

(26) Brady, J. P.; Farber, P. J.; Sekhar, A.; Lin, Y.-H.; Huang, R.; Bah, A.; Nott, T. J.; Chan, H. S.; Baldwin, A. J.; Forman-Kay, J. D.; others Structural and hydrodynamic

properties of an intrinsically disordered region of a germ cell-specific protein on phase separation. *Proc. Natl. Acad. Sci. U.S.A.* **2017**, *114*, E8194–E8203.

(27) Yokosawa, K.; Kajimoto, S.; Shibata, D.; Kuroi, K.; Konno, T.; Nakabayashi, T. Concentration Quantification of the Low-Complexity Domain of Fused in Sarcoma inside a Single Droplet and Effects of Solution Parameters. *J. Phys. Chem. Lett.* **2022**, *13*, 5692–5697.

(28) Abyzov, A.; Blackledge, M.; Zweckstetter, M. Conformational dynamics of intrinsically disordered proteins regulate biomolecular condensate chemistry. *Chem. Rev.* **2022**, *122*, 6719–6748.

(29) Murthy, A. C.; Fawzi, N. L. The (un)structural biology of biomolecular liquid-liquid phase separation using NMR spectroscopy. *J. Biol. Chem.* **2020**, *295*, 2375–2384.

(30) Taylor, N. O.; Wei, M.-T.; Stone, H. A.; Brangwynne, C. P. Quantifying dynamics in phase-separated condensates using fluorescence recovery after photobleaching. *Biophys. J.* **2019**, *117*, 1285–1300.

(31) Nott, T. J.; Petsalaki, E.; Farber, P.; Jervis, D.; Fussner, E.; Plochowietz, A.; Craggs, T. D.; Bazett-Jones, D. P.; Pawson, T.; Forman-Kay, J. D.; others Phase transition of a disordered nuage protein generates environmentally responsive membraneless organelles. *Mol. Cell* **2015**, *57*, 936–947.

(32) König, I.; Zarrine-Afsar, A.; Aznauryan, M.; Soranno, A.; Wunderlich, B.; Dingfelder, F.; Stüber, J. C.; Plückthun, A.; Nettels, D.; Schuler, B. Single-molecule spectroscopy of protein conformational dynamics in live eukaryotic cells. *Nat. Meth.* **2015**, *12*, 773–779.

(33) König, I.; Soranno, A.; Nettels, D.; Schuler, B. Impact of in-cell and in-vitro crowding on the conformations and dynamics of an intrinsically disordered protein. *Angew. Chem. Int. Ed.* **2021**, *60*, 10724–10729.

(34) Feng, Z.; Chen, X.; Wu, X.; Zhang, M. Formation of biological condensates via phase separation: Characteristics, analytical methods, and physiological implications. *J. Biol. Chem.* **2019**, *294*, 14823–14835.

(35) Chebaro, Y.; Ballard, A. J.; Chakraborty, D.; Wales, D. J. Intrinsically disordered energy landscapes. *Sci. Rep.* **2015**, *5*, 10386.

(36) Csizmok, V.; Follis, A. V.; Kriwacki, R. W.; Forman-Kay, J. D. Dynamic protein interaction networks and new structural paradigms in signaling. *Chem. Rev.* **2016**, *116*, 6424–6462.

(37) Schneider, R.; Blackledge, M.; Jensen, M. R. Elucidating binding mechanisms and dynamics of intrinsically disordered protein complexes using NMR spectroscopy. *Curr. Opin. Struct. Biol.* **2019**, *54*, 10–18.

(38) Dyson, H. J.; Wright, P. E. Coupling of folding and binding for unstructured proteins. *Curr. Opin. Struct. Biol.* **2002**, *12*, 54–60.

(39) Tompa, P.; Fuxreiter, M. Fuzzy complexes: polymorphism and structural disorder in protein–protein interactions. *Trends Biochem. Sci.* **2008**, *33*, 2–8.

(40) Fuxreiter, M.; Simon, I.; Friedrich, P.; Tompa, P. Preformed structural elements feature in partner recognition by intrinsically unstructured proteins. *J. Mol. Biol.* **2004**, *338*, 1015–1026.

(41) Shoemaker, B. A.; Portman, J. J.; Wolynes, P. G. Speeding molecular recognition by using the folding funnel: the fly-casting mechanism. *Proc. Natl. Acad. Sci. U.S.A.* **2000**, *97*, 8868–8873.

(42) Galvanetto, N.; Ivanović, M. T.; Chowdhury, A.; Sottini, A.; Nüesch, M. F.; Nettels, D.; Best, R. B.; Schuler, B. Extreme dynamics in a biomolecular condensate. *Nature* **2023**, *619*, 876–883.

(43) Guseva, S.; Schnapka, V.; Adamski, W.; Maurin, D.; Ruigrok, R. W. H.; Salvi, N.; Blackledge, M. Liquid–Liquid Phase Separation Modifies the Dynamic Properties of Intrinsically Disordered Proteins. *J. Am. Chem. Soc.* **2023**, *145*, 10548–10563.

(44) Benayad, Z.; von Bülow, S.; Stelzl, L. S.; Hummer, G. Simulation of FUS protein condensates with an adapted coarse-grained model. *J. Chem. Theory Comput.* **2021**, *17*, 525–537.

(45) Rauscher, S.; Pomés, R. The liquid structure of elastin. *eLife* **2017**, *6*, e26526.

(46) Brangwynne, C. P.; Mitchison, T. J.; Hyman, A. A. Active liquid-like behavior of nucleoli determines their size and shape in Xenopus laevis oocytes. *Proc. Natl. Acad. Sci. U.S.A.* **2011**, *108*, 4334–4339.

(47) Peran, I.; Mittag, T. Molecular structure in biomolecular condensates. *Curr. Opin. Struct. Biol.* **2020**, *60*, 17–26.

(48) Fischer, A. A. M.; Robertson, H. B.; Kong, D.; Grimm, M. M.; Grether, J.; Groth, J.; Baltes, C.; Fliegauf, M.; Lautenschläger, F.; Grimbacher, B.; Ye, H.; Helms, V.; Weber, W. Engineering Material Properties of Transcription Factor Condensates to Control Gene Expression in Mammalian Cells and Mice. *Small* 2311834.

(49) Kitahara, R.; Yamazaki, R.; Ide, F.; Li, S.; Shiramasa, Y.; Sasahara, N.; Yoshizawa, T. Pressure-Jump Kinetics of Liquid–Liquid Phase Separation: Comparison of Two Different Condensed Phases of the RNA-Binding Protein, Fused in Sarcoma. *J. Am. Chem. Soc.* **2021**, *143*, 19697–19702.

(50) Guo, W.; Naujock, M.; Fumagalli, L.; Vandoorne, T.; Baatsen, P.; Boon, R.; Ordovás, L.; Patel, A.; Welters, M.; Vanwelden, T.; others HDAC6 inhibition reverses axonal transport defects in motor neurons derived from FUS-ALS patients. *Nat. Commun.* **2017**, *8*, 861.

(51) Kamelgarn, M.; Chen, J.; Kuang, L.; Jin, H.; Kasarskis, E. J.; Zhu, H. ALS mutations of FUS suppress protein translation and disrupt the regulation of nonsense-mediated decay. *Proc. Natl. Acad. Sci. U.S.A.* **2018**, *115*, E11904–E11913.

(52) Rulten, S. L.; Rotheray, A.; Green, R. L.; Grundy, G. J.; Moore, D. A. Q.; Gómez-Herreros, F.; Hafezparast, M.; Caldecott, K. W. PARP-1 dependent recruitment of the amyotrophic lateral sclerosis-associated protein FUS/TLS to sites of oxidative DNA damage. *Nucleic Acids Res.* **2013**, *42*, 307–314.

(53) Murakami, T.; Qamar, S.; Lin, J. Q.; Schierle, G. S. K.; Rees, E.; Miyashita, A.; Costa, A. R.; Dodd, R. B.; Chan, F. T.; Michel, C. H.; others ALS/FTD mutation-induced phase transition of FUS liquid droplets and reversible hydrogels into irreversible hydrogels impairs RNP granule function. *Neuron* **2015**, *88*, 678–690.

(54) Avni, A.; Joshi, A.; Walimbe, A.; Pattanashetty, S. G.; Mukhopadhyay, S. Single-droplet surface-enhanced Raman scattering decodes the molecular determinants of liquid-liquid phase separation. *Nat. Commun.* **2022**, *13*, 4378.

(55) Rekhi, S.; Garcia, C. G.; Barai, M.; Rizuan, A.; Schuster, B. S.; Kiick, K. L.; Mittal, J. Expanding the molecular language of protein liquid–liquid phase separation. *Nat. Chem.* **2024**,

(56) Vitkup, D.; Ringe, D.; Petsko, G. A.; Karplus, M. Solvent mobility and the protein'glass' transition. *Nat. Struct. Biol.* **2000**, *7*, 34–38.

(57) Li, T.; Hassanali, A. A.; Kao, Y.-T.; Zhong, D.; Singer, S. J. Hydration dynamics and time scales of coupled water- protein fluctuations. *J. Am. Chem. Soc.* **2007**, *129*, 3376–3382.

(58) Frauenfelder, H.; Chen, G.; Berendzen, J.; Fenimore, P. W.; Jansson, H.; McMahon, B. H.; Stroe, I. R.; Swenson, J.; Young, R. D. A unified model of protein dynamics. *Proc. Natl. Acad. Sci. U.S.A* **2009**, *106*, 5129–5134.

(59) Mukherjee, S.; Mondal, S.; Bagchi, B. Mechanism of Solvent Control of Protein Dynamics. *Phys. Rev. Lett.* **2019**, *122*, 058101.

(60) Mukherjee, S.; Mondal, S.; Bagchi, B. Distinguishing dynamical features of water inside protein hydration layer: Distribution reveals what is hidden behind the average. *J. Chem. Phys.* **2017**, *147*, 024901.

(61) Päslack, C.; Schäfer, L. V.; Heyden, M. Protein flexibility reduces solvent-mediated friction barriers of ligand binding to a hydrophobic surface patch. *Phys. Chem. Chem. Phys.* **2021**, *23*, 5665–5672.

(62) Schirò, G.; Weik, M. Role of hydration water in the onset of protein structural dynamics. *J. Phys. Condens. Matter* **2019**, *31*, 463002.

(63) Mondal, S.; Bagchi, B. From structure and dynamics to biomolecular functions: The ubiquitous role of solvent in biology. *Curr. Opin. Struct. Biol.* **2022**, *77*, 102462.

(64) Reid, K. M.; Singh, A. K.; Bikash, C. R.; Wei, J.; Tal-Gan, Y.; Vinh, N. Q.; Leitner, D. M. The origin and impact of bound water around intrinsically disordered proteins. *Biophys. J.* **2022**, *121*, 540–551.

(65) Fisette, O.; Päslack, C.; Barnes, R.; Isas, J. M.; Langen, R.; Heyden, M.; Han, S.; Schäfer, L. V. Hydration dynamics of a peripheral membrane protein. *J. Am. Chem. Soc.* **2016**, *138*, 11526–11535.

(66) Persson, R. A.; Pattni, V.; Singh, A.; Kast, S. M.; Heyden, M. Signatures of solvation thermodynamics in spectra of intermolecular vibrations. *J. Chem. Theory Comput.* **2017**, *13*, 4467–4481.

(67) Heyden, M. Disassembling solvation free energies into local contributions – Toward a microscopic understanding of solvation processes. *WIREs Comput. Mol. Sci.* **2019**, *9*, e1390.

(68) Päslack, C.; Das, C. K.; Schlitter, J.; Schäfer, L. V. Spectrally resolved estimation of water entropy in the active site of human carbonic anhydrase II. *J. Chem. Theory Comput.* **2021**, *17*, 5409–5418.

(69) Mukherjee, S.; Schäfer, L. V. Spatially Resolved Hydration Thermodynamics in Biomolecular Systems. *J. Phys. Chem. B* **2022**, *126*, 3619–3631.

(70) Mukherjee, S.; Schäfer, L. V. Thermodynamic forces from protein and water govern condensate formation of an intrinsically disordered protein domain. *Nat. Commun.* **2023**, *14*, 5892.

(71) Mukherjee, S.; Ramos, S.; Pezzotti, S.; Kalarikkal, A.; Prass, T. M.; Galazzo, L.; Gendreizig, D.; Barbosa, N.; Bordignon, E.; Havenith, M.; Schäfer, L. V. Entropy Tug-of-War Determines Solvent Effects in the Liquid–Liquid Phase Separation of a Globular Protein. *J. Phys. Chem. Lett.* **2024**, *15*, 4047–4055.

(72) Krevert, C. S.; Chavez, D.; Chatterjee, S.; Stelzl, L. S.; Pütz, S.; Roeters, S. J.; Rudzinski, J. F.; Fawzi, N. L.; Girard, M.; Parekh, S. H.; Hunger, J. Liquid–Liquid Phase Separation of the Intrinsically Disordered Domain of the Fused in Sarcoma Protein Results in Substantial Slowing of Hydration Dynamics. *J. Phys. Chem. Lett.* **2023**, *14*, 11224–11234.

(73) Lorenz-Ochoa, K. A.; Baiz, C. R. Ultrafast Spectroscopy Reveals Slow Water Dynamics in Biocondensates. *J. Am. Chem. Soc.* **2023**, *145*, 27800–27809.

Supporting Information: Heterogeneous Slowdown of Dynamics in the Condensate of an Intrinsically Disordered Protein

Saumyak Mukherjee and Lars V. Schäfer*

Center for Theoretical Chemistry, Ruhr University Bochum, D-44780 Bochum, Germany

E-mail: lars.schaefer@ruhr-uni-bochum.de

Methods

System preparation

The intrinsically disordered low complexity domain (LCD) of the human Fused in Sarcoma (FUS) RNA-binding protein (UniProt ID: P3563, residues 1 to 163 of a total 526 residues) was simulated in this study. The initial atomic coordinates of FUS-LCD were generated using AlphaFold,[S1,S2] which predicted an extended conformation without any secondary structure.

As explained in detail in our previous work,[S3] the initial equilibrated condensate system at a protein concentration of 350 mg ml^{-1} was obtained from coarse-grained (CG) MD simulations with the Martini 2.2[S4] force field. Scaled protein-protein Lennard-Jones (LJ) interactions were used to maintain the liquidlike dynamical features of the condensate, as suggested by Benayad et al.[S5] Eight copies of the coarse-grained FUS-LCD chain were inserted in a cubic periodic simulation box along with 4366 CG water beads (1 Martini water bead corresponds to 4 atomistic water molecules) and 16 sodium ions to neutralize the net charge of the simulation box.

The system was energy minimized and simulated for 1 μs under NpT conditions at $T =$ 300 K and $p = 1$ bar. The resulting box dimensions were 8.9 nm. Temperature and pressure were maintained using a weak coupling thermostat and barostat,[S6] respectively. The coarse-grained simulations were performed using the recommended settings,[S7] which included the use of a 1.1 nm cut-off for the non-bonded interactions and a 20 fs time step to integrate the equations of motion.

The CG simulations enabled fast equilibration of the protein configurations. However, realistic dynamical data (time scales) can not be obtained from this approach. Hence, the CG simulations were only used for initial equilibration but not for analysis. All production simulations were performed with the all-atom force field amber99SB-disp.[S8] First, the systems obtained from CG equilibration were back-mapped to the all-atom level using the `initram.sh` and `backward.py` scripts.[S9] The resulting atomistic proteins were solvated with 16509 water molecules. 79 sodium and 63 chloride ions were added to neutralize the charges from the protein chains and to have a salt concentration of 150 mM, corresponding to physiological ion concentrations. The protein, water and ions were described by the a99SB-disp force field (and the corresponding 4-point water model derived from TIP4P-D),[S8] which was shown to be a good choice for FUS in a recent study.[S10]

A reference dilute system was also simulated. It included a single FUS-LCD chain in 45681 water molecules along with 134 sodium and 132 chloride ions in a 11.2 nm cubic periodic box. The salt concentration in this case was also 150 mM. Snapshots of the dilute and condensate systems are shown in Figs. S1A and S1B respectively.

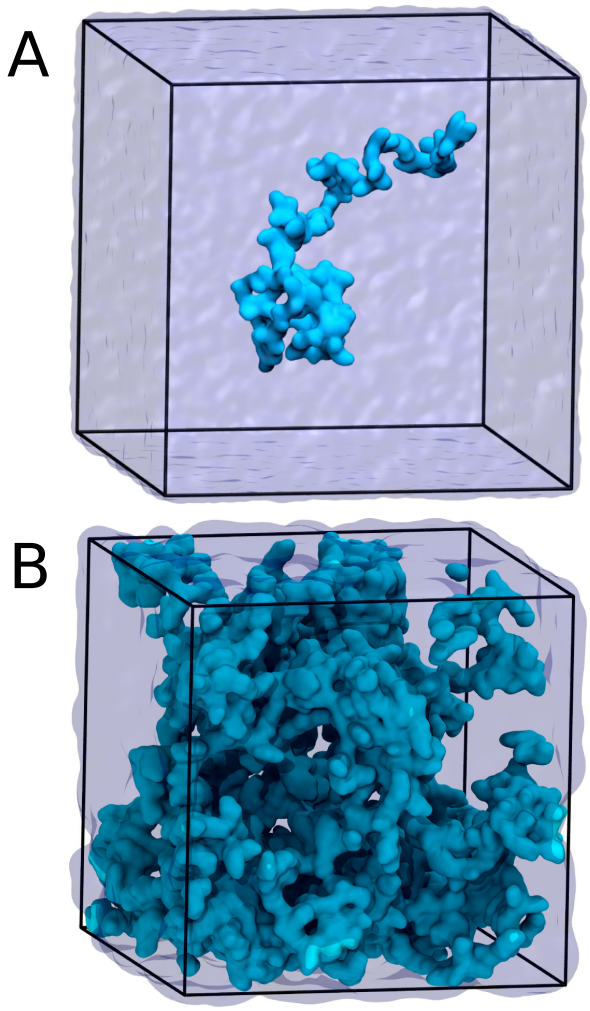

Figure S1: Representative snapshots of the equilibrated systems of (A) dilute and (B) condensate phases.

Simulation details

All simulations were performed using the GROMACS (version 2021.1) molecular dynamics simulation package.[S11] Both the systems were first energy minimized using the steepest descent algorithm and then equilibrated with harmonic position restraints on the protein backbone for 10 ns (restraining force constants of 1000 kJ mol^{-1} nm^{-2}) under NpT conditions at T = 300 K and p = 1 bar. This was followed by further NpT equilibration under the same conditions for 100 ns without any position restraints. Thereafter, the systems were equilibrated for 100 ns at constant volume, followed by the final production runs for 1 μs in

the NVT ensemble. Coordinates were saved to disk every 10 ps. For the analysis of water dynamics, 100 ns production runs were performed with a data dumping frequency of 1 ps. In these simulations, the velocity rescaling thermostat with a stochastic term[S12] and the Berendsen barostat[S6] were used to control temperature and pressure, respectively.

All atomistic MD simulations were done using the leap-frog integrator with a time step of 2 fs. Protein bonds and internal degrees of water molecules were constrained using the LINCS and SETTLE algorithms, respectively. Short-range electrostatic and Lennard-Jones interactions were calculated up to an interparticle distance cut-off of 1.0 nm. Long-range electrostatic interactions were treated with the particle-mesh Ewald technique[S13] with a grid spacing of 0.12 nm.

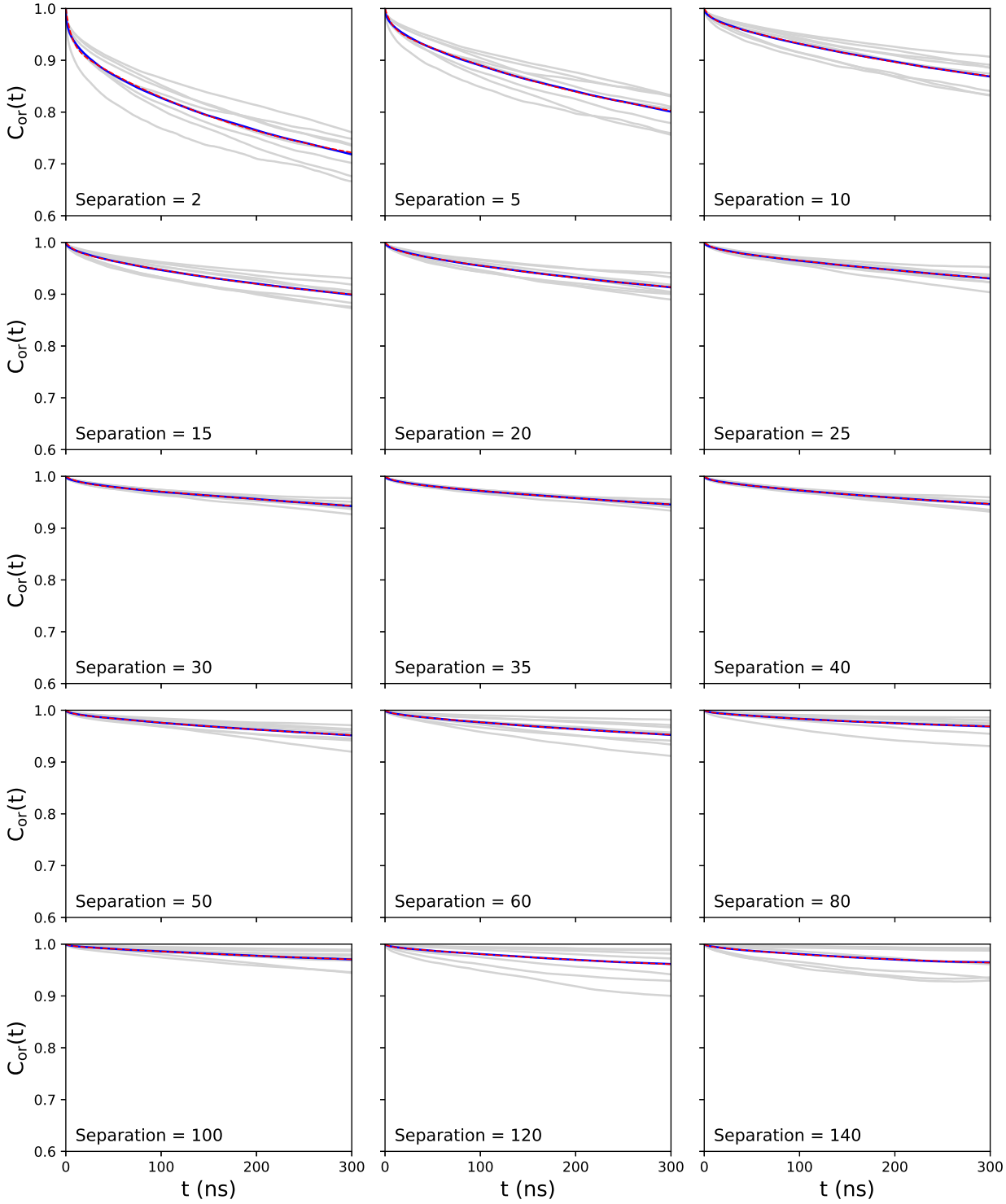

Figure S2: Orientational autocorrelation functions of the $C_\alpha - C_\alpha$ vectors at selected separations in the condensate system. The light grey curves represent the 8 individual proteins in the system. The bold blue line is the average ACF over the 8 individual ones. The dashed red line denotes the biexponential fit to the mean ACF.

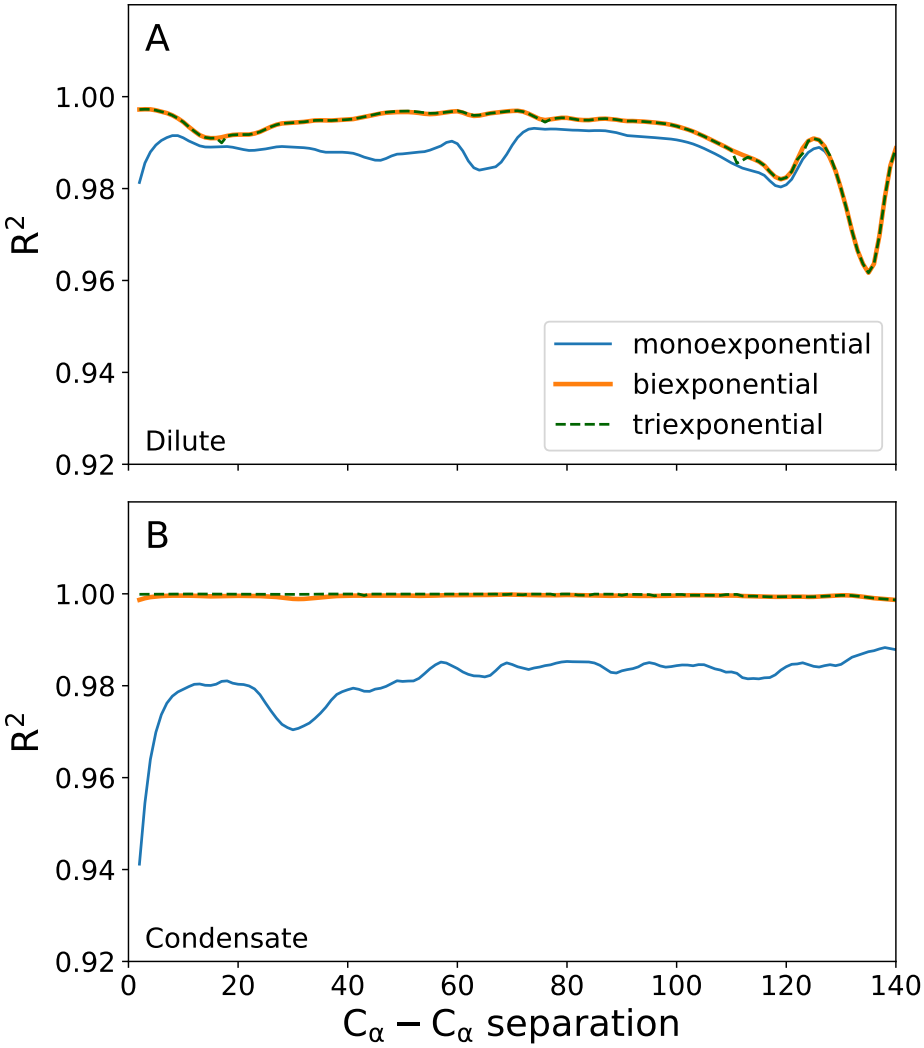

Figure S3: Coefficient of determination (R^2) for mono-, bi-, and triexponential fits of the ACFs of $C_\alpha - C_\alpha$ vector orientation dynamics as a function of $C_\alpha - C_\alpha$ separation in (A) dilute and (B) condensate systems.

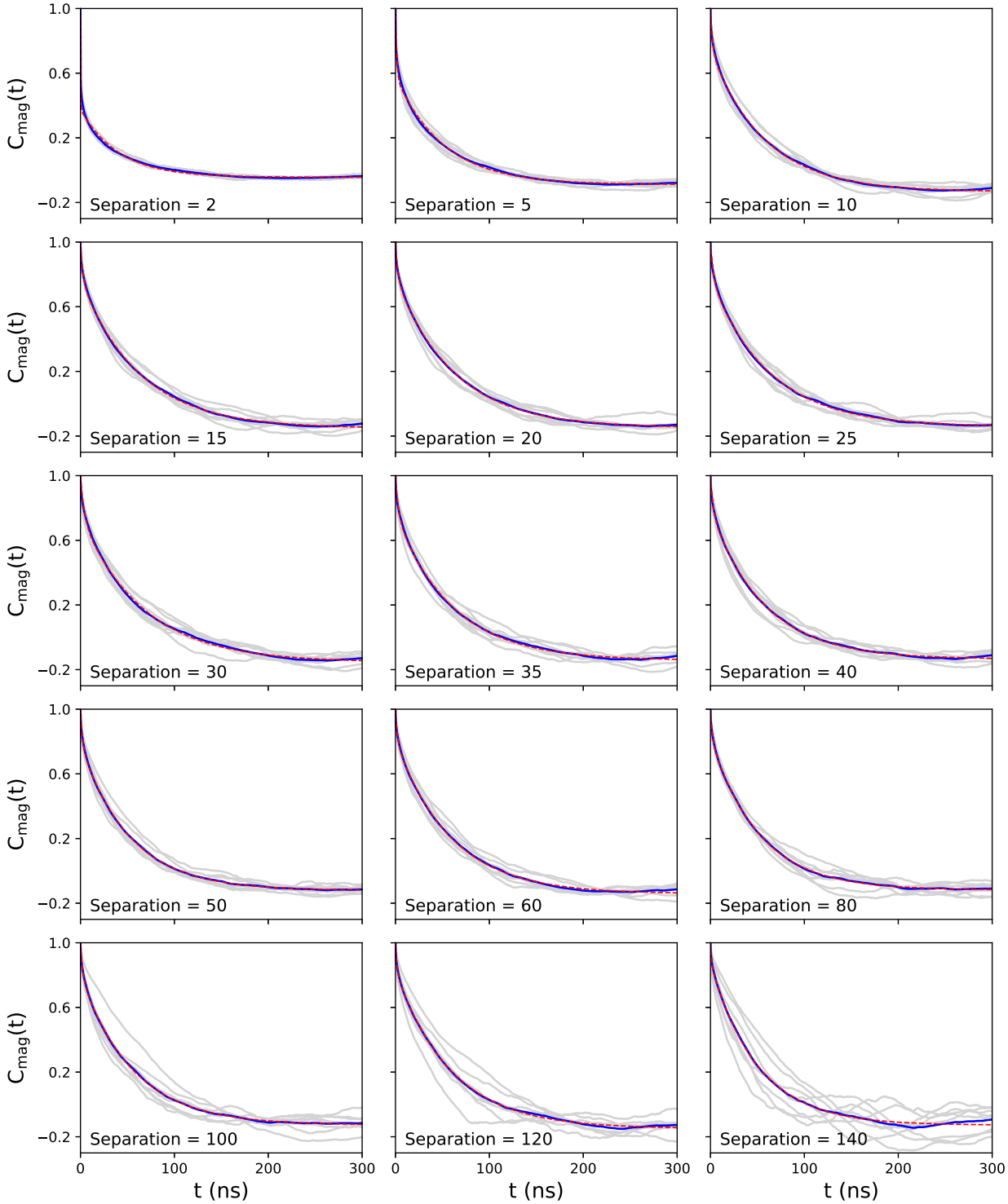

Figure S4: Magnitude or distance autocorrelation functions of the $C_\alpha - C_\alpha$ vectors at selected separations in the condensate system. The light grey curves represent the 8 individual proteins in the system. The bold blue line is the average ACF over the 8 individual ones. The dashed red line denotes the biexponential fit to the mean ACF.

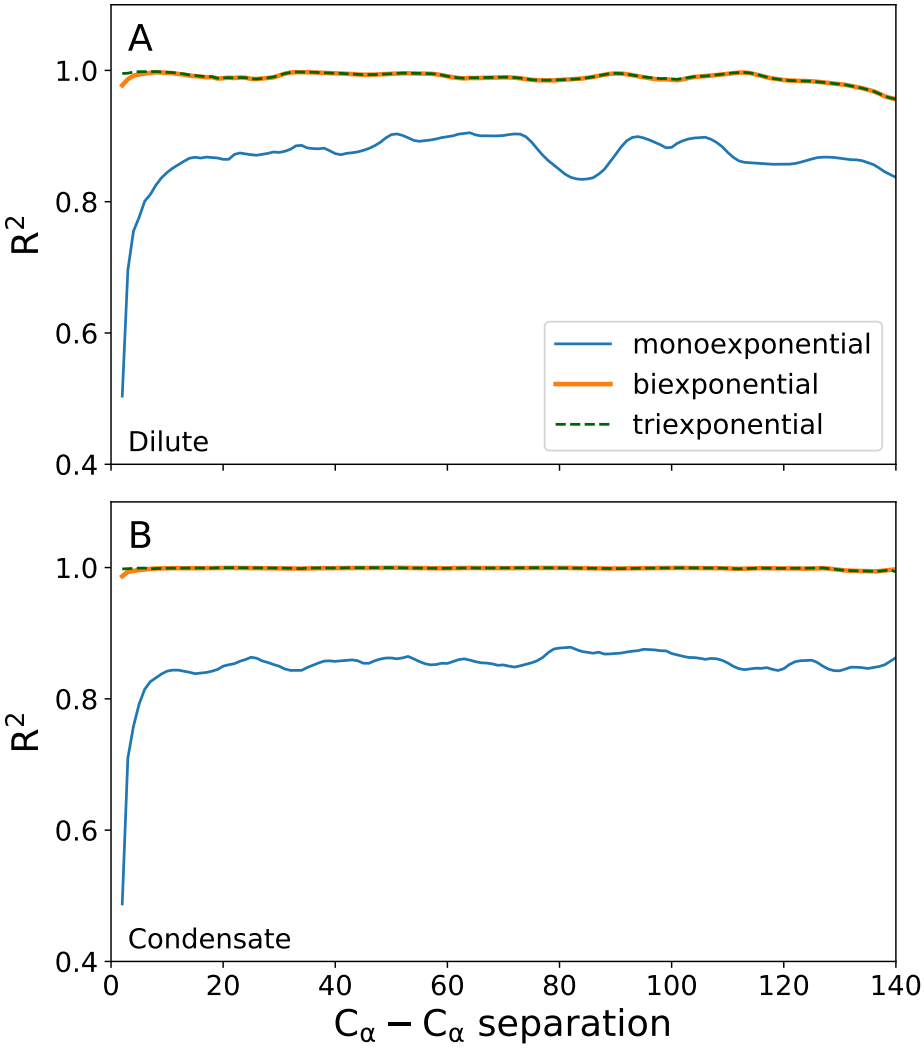

Figure S5: Coefficient of determination (R^2) for mono-, bi-, and triexponential fits of the ACFs of $C_\alpha - C_\alpha$ vector magnitude fluctuation dynamics as a function of $C_\alpha - C_\alpha$ separation in (A) dilute and (B) condensate systems.

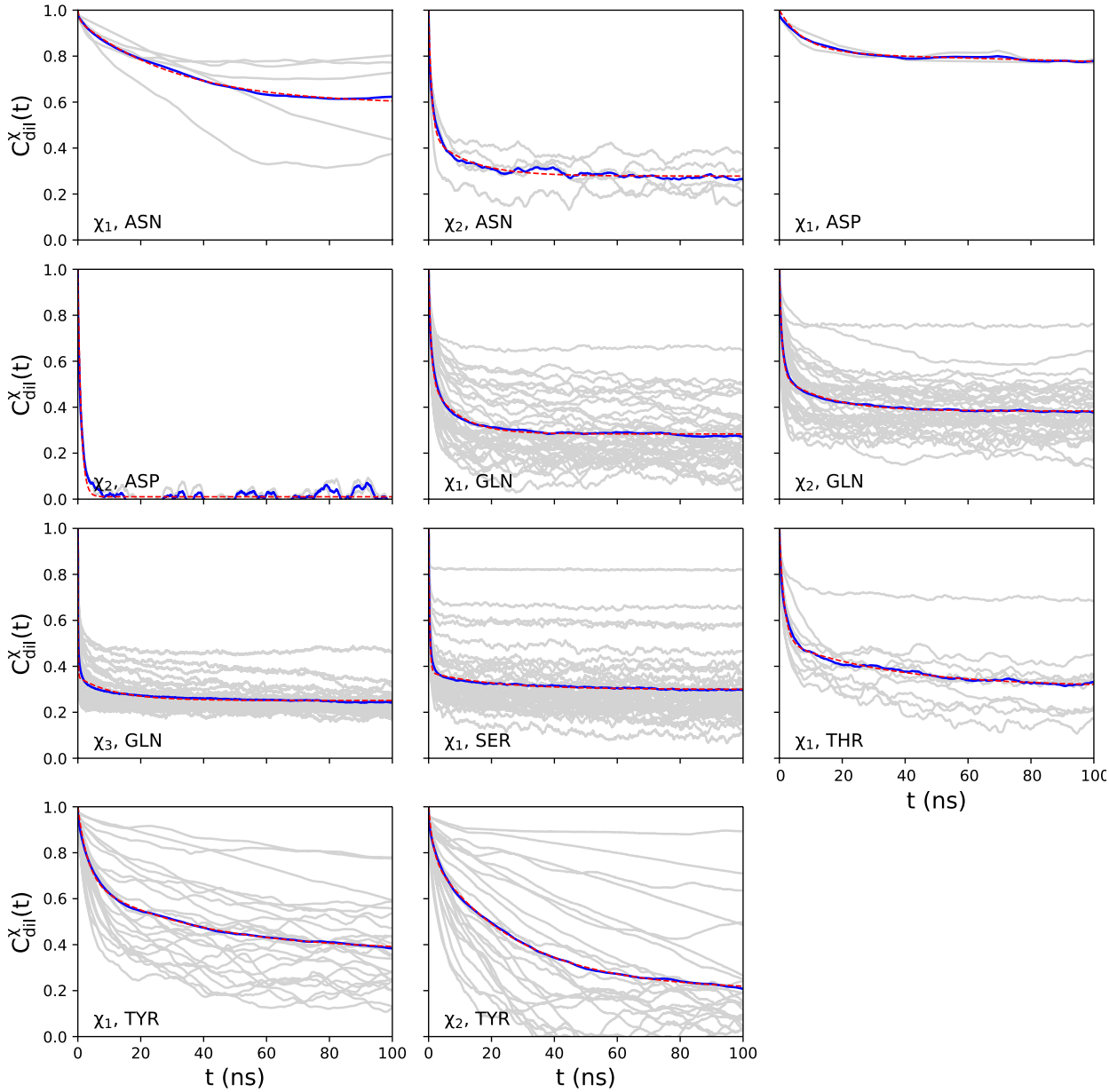

Figure S6: Side-chain dihedral autocorrelation functions of the protein in the dilute system. The light grey curves represent the individual side-chains of the same type present in the system. The bold blue line is the average ACF. The dashed red line denotes the biexponential fit to the mean ACF.

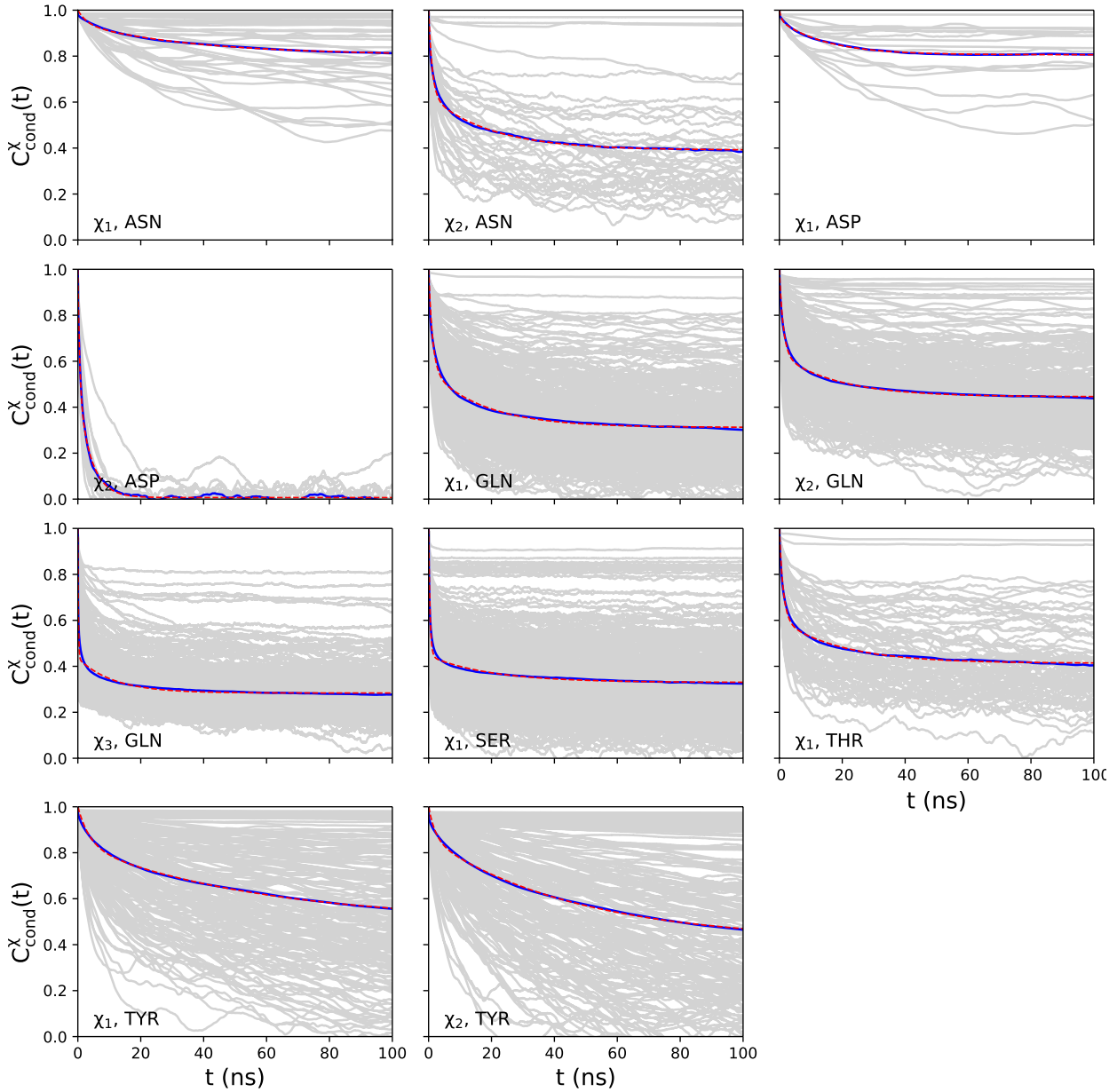

Figure S7: Side-chain dihedral autocorrelation functions of the protein in the condensate system. The light grey curves represent the individual side-chains of the same type present in the system. The bold blue line is the average ACF. The dashed red line denotes the biexponential fit to the mean ACF.

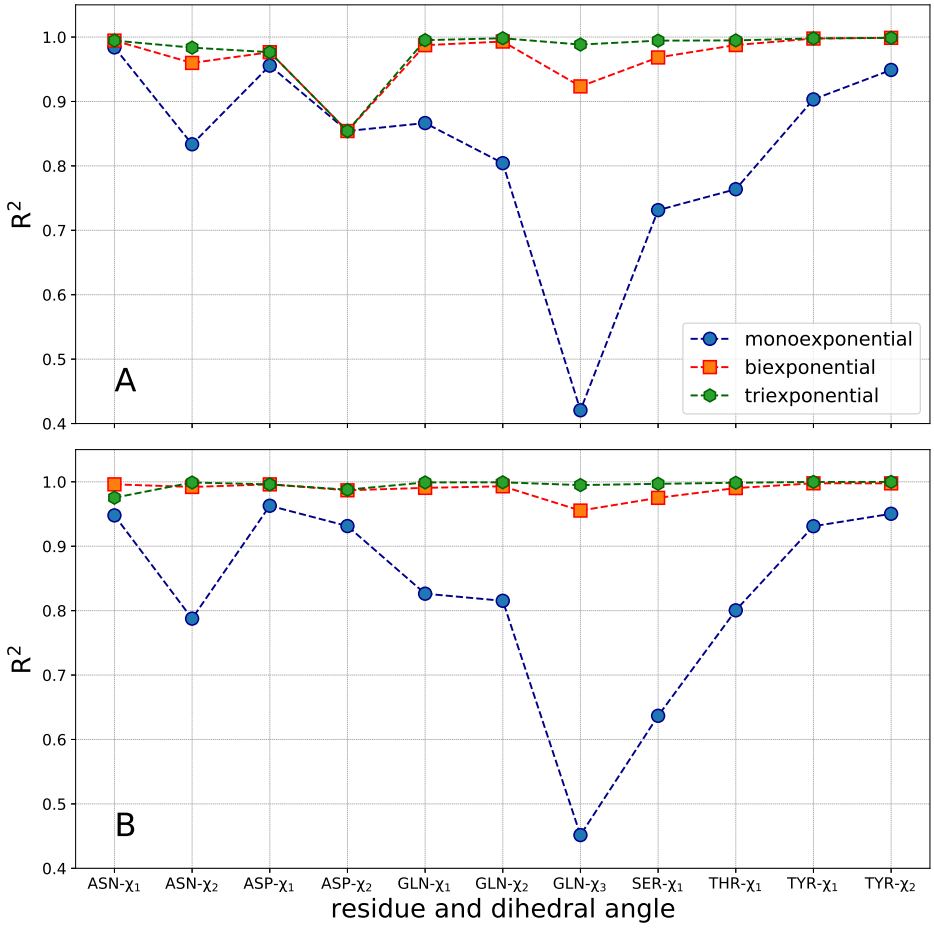

Figure S8: Coefficient of determination (R^2) for mono-, bi-, and triexponential fits of the ACFs of dihedral rotations ($\chi_1, \chi_2, and \chi_3$) of respective residues present in the (A) dilute and the (B) condensate systems.

References

(S1) Jumper, J.; Evans, R.; Pritzel, A.; Green, T.; Figurnov, M.; Ronneberger, O.; Tunyasuvunakool, K.; Bates, R.; Žídek, A.; Potapenko, A.; others Highly accurate protein structure prediction with AlphaFold. *Nature* **2021**, *596*, 583–589.

(S2) Varadi, M.; Anyango, S.; Deshpande, M.; Nair, S.; Natassia, C.; Yordanova, G.; Yuan, D.; Stroe, O.; Wood, G.; Laydon, A.; others AlphaFold Protein Structure Database: Massively expanding the structural coverage of protein-sequence space with high-accuracy models. *Nucleic Acids Res.* **2022**, *50*, D439–D444.

(S3) Mukherjee, S.; Schäfer, L. V. Thermodynamic forces from protein and water govern condensate formation of an intrinsically disordered protein domain. *Nat. Commun.* **2023**, *14*, 5892.

(S4) de Jong, D. H.; Singh, G.; Bennett, W. F. D.; Arnarez, C.; Wassenaar, T. A.; Schäfer, L. V.; Periole, X.; Tieleman, D. P.; Marrink, S. J. Improved parameters for the Martini coarse-grained protein force field. *J. Chem. Theory Comput.* **2013**, *9*, 687–697.

(S5) Benayad, Z.; von Bülow, S.; Stelzl, L. S.; Hummer, G. Simulation of FUS protein condensates with an adapted coarse-grained model. *J. Chem. Theory Comput.* **2021**, *17*, 525–537.

(S6) Berendsen, H. J. C.; Postma, J. P. M.; van Gunsteren, W. F.; DiNola, A.; Haak, J. R. Molecular dynamics with coupling to an external bath. *J. Chem. Phys.* **1984**, *81*, 3684–3690.

(S7) de Jong, D. H.; Baoukina, S.; Ingólfsson, H. I.; Marrink, S. J. Martini straight: Boosting performance using a shorter cutoff and GPUs. *Comput. Phys. Commun.* **2016**, *199*, 1–7.

(S8) Robustelli, P.; Piana, S.; Shaw, D. E. Developing a molecular dynamics force field for both folded and disordered protein states. *Proc. Natl. Acad. Sci. U.S.A.* **2018**, *115*, E4758–E4766.

(S9) Wassenaar, T. A.; Pluhackova, K.; Böckmann, R. A.; Marrink, S. J.; Tieleman, D. P. Going backward: a flexible geometric approach to reverse transformation from coarse grained to atomistic models. *J. Chem. Theory Comput.* **2014**, *10*, 676–690.

(S10) Sarthak, K.; Winogradoff, D.; Ge, Y.; Myong, S.; Aksimentiev, A. Benchmarking Molecular Dynamics Force Fields for All-Atom Simulations of Biological Condensates. *J. Chem. Theory Comput.* **2023**, *12*, 3721–3740.

(S11) Abraham, M. J.; Murtola, T.; Schulz, R.; Páll, S.; Smith, J. C.; Hess, B.; Lindahl, E. GROMACS: High performance molecular simulations through multi-level parallelism from laptops to supercomputers. *SoftwareX* **2015**, *1*, 19–25.

(S12) Bussi, G.; Donadio, D.; Parrinello, M. Canonical sampling through velocity rescaling. *J. Chem. Phys.* **2007**, *126*, 014101.

(S13) Darden, T.; York, D.; Pedersen, L. Particle mesh Ewald: An Nlog(N) method for Ewald sums in large systems. *J. Chem. Phys.* **1993**, *98*, 10089–10092.